

# The effect of compliant prisms on subduction zone earthquakes and tsunamis

Gabriel C. Lotto<sup>a,1</sup>, Eric M. Dunham<sup>a,b</sup>, Tamara N. Jeppson<sup>c</sup>, Harold J. Tobin<sup>c</sup>

a. Department of Geophysics, Stanford University, Stanford, CA, USA

b. Institute for Computational and Mathematical Engineering, Stanford University, Stanford, CA, USA

c. Geoscience Department, University of Wisconsin – Madison, Madison, WI, USA

1. Corresponding Author: [glotto@stanford.edu](mailto:glotto@stanford.edu)

October 7, 2016

## Abstract

Earthquakes generate tsunamis by coseismically deforming the seafloor, and that deformation is largely controlled by the shallow rupture process. Therefore, in order to better understand how earthquakes generate tsunamis, one must consider the material structure and frictional properties of the shallowest part of the subduction zone, where ruptures often encounter compliant sedimentary prisms. Compliant prisms have been associated with enhanced shallow slip, seafloor deformation, and tsunami heights, particularly in the context of tsunami earthquakes. To rigorously quantify the role compliant prisms play in generating tsunamis, we perform a series of numerical simulations that directly couple dynamic rupture on a dipping thrust fault to the elastodynamic response of the Earth and the acoustic response of the ocean. Gravity is included in our simulations in the context of a linearized Eulerian description of the ocean, which allows us to model tsunami generation and propagation, including dispersion and related nonhydrostatic effects. Our simulations span a three-dimensional parameter space of prism size, prism compliance, and sub-prism friction – specifically, the rate-and-state parameter  $b - a$  that determines velocity-weakening or velocity-strengthening behavior. We find that compliant prisms generally slow rupture velocity and, for larger prisms, generate tsunamis more efficiently than subduction zones without prisms. In most but not all cases, larger, more compliant prisms cause greater amounts of shallow slip and larger tsunamis. Furthermore, shallow friction is also quite important in determining overall slip; increasing sub-prism  $b - a$  enhances slip everywhere along the fault. Counterintuitively, we find that in simulations with large prisms and velocity-strengthening

27 friction at the base of the prism, increasing prism compliance reduces rather than  
28 enhances shallow slip and tsunami wave height.

29 Keywords: tsunami, compliant prism, tsunami earthquake, subduction zone, dynamic  
30 rupture

31 Funding: This work was supported by the National Science Foundation (EAR-1255439)  
32 and the Alfred P. Sloan Foundation (BR2012-097).

## 33 1 Introduction

34 Tsunamis induced by subduction zone earthquakes can be incredibly destructive events.  
35 Within the past few decades, tsunamis have been among the deadliest and costliest natural  
36 hazards [42], killing hundreds of thousands of people and doing billions of dollars of damage.  
37 Our study addresses tsunamigenic earthquakes by using dynamic rupture models to explore  
38 how the unique shallow structure of subduction zones, specifically sedimentary prisms, in-  
39 fluences the rupture process and tsunami generation. To motivate this effort, we provide  
40 a brief overview of tsunamigenic earthquakes, as well as the current understanding of the  
41 material structure near the trench and frictional properties of the shallow plate interface,  
42 particularly as these relate to tsunami generation.

43 Tsunamigenic earthquakes can be broken into two major categories: great megathrust  
44 events and tsunami earthquakes [19]. The former category includes the 26 December 2004  
45 Sumatra earthquake [43] and the 11 March 2011 Tohoku-Oki earthquake [41], both  $M_w$   
46 9.0+ earthquakes that generated large amounts of coseismic slip. The latter category in-  
47 cludes events like the 17 July 2006 Java earthquake [1] and the 25 October 2010 Mentawai  
48 earthquake [28], which excited unusually large tsunamis for their body- and surface-wave  
49 magnitudes.

50 Coseismic slip during the Tohoku-Oki event displaced the seafloor near the Japan Trench  
51 by about 50 meters, according to bathymetric surveys, GPS measurements, and acoustic  
52 ranging data [10, 39]. Seismic reflection data recorded days after the earthquake showed  
53 deformation in the sediments near the trench, indicating that fault rupture reached all the  
54 way to the seafloor [23]. Numerical modeling results indicate that rupture to the trench could  
55 occur even with shallow frictional conditions unfavorable to earthquake nucleation [26]. It  
56 is less clear that the Sumatra earthquake ruptured to the seafloor, as slip inversions with  
57 primarily deeper slip patches fit the sparse seismic and geodetic data reasonably well [5, 35].  
58 However, any slip that did occur near the trench could have contributed substantially to the  
59 resulting tsunami [13, 15].

60 Tsunami earthquakes, first identified by Kanamori [19] in reference to the 1896 Sanriku,  
61 Japan, earthquake and the 1946 Aleutian Islands earthquake, also exhibit coseismic rupture  
62 through the shallow parts of subduction zones. Polet and Kanamori [36] identified several  
63 additional characteristics that tsunami earthquakes share: a slow rupture velocity that in-  
64 efficiently releases high-frequency energy, a large distance between the earthquake source  
65 and the land, a subducting sedimentary layer with a small (under 40 km downdip width)  
66 accretionary prism at the trench, and rupture that propagates to very shallow depths. The  
67 most common explanation for the occurrence of tsunami earthquakes invokes the ease of  
68 deforming compliant accretionary prisms and subducted sediments, which are often present  
69 at subduction zone trenches [20, 36, 44].

70 Generally speaking, the mechanism behind enhanced deformation in a compliant zone is  
71 that, in accordance with Hooke’s Law, a given earthquake-induced stress change will cause  
72 greater strain and hence greater displacement in a more compliant material. In addition  
73 to the increased strain expected in the compliant prism, normal stress changes due to the  
74 presence of a bimaterial interface can affect the rupture process and facilitate unstable slip  
75 [2, 50]. Ma and Beroza [30] found that normal stress variations on a dipping thrust fault due  
76 to free surface and bimaterial effects can create larger-than-normal stress drops when the  
77 hanging wall material is more compliant. However, material properties may not be solely  
78 responsible for large tsunamis; Bilek and Lay [3] pointed out that tsunami earthquakes  
79 have occurred both in regions with and without large sedimentary prisms, suggesting that  
80 frictional properties on the plate interface may also influence the rupture process.

81 Frictional properties are an important factor in determining rupture behavior on faults,  
82 but the frictional properties of the materials beneath subduction zone prisms are not fully  
83 understood. The conventional view of plate interfaces is that they are seismogenic only  
84 below a depth of about 5-10 kilometers [16]. Below this depth, fault materials have velocity-  
85 weakening properties (they decrease in strength with increased slip velocity) and earth-  
86 quakes can nucleate; above, unconsolidated clay-rich fault gouge is thought to be velocity-  
87 strengthening, inhibiting unstable slip. Our understanding of the upper limit of unstable  
88 slip is based in part on experiments showing that smectite-rich clay sediments dehydrate to  
89 form illite-rich material at  $\sim 150$  °C [14]. But experiments have shown that illite fault gouge  
90 may have velocity-strengthening properties [38]. Ultimately, it is likely that the depth range  
91 of velocity-weakening behavior is controlled by a combination of sediment composition, tem-  
92 perature, pore fluid pressure, and effective normal stress [7]. As a practical example from a  
93 real subduction zone, laboratory experiments on samples from the pelagic clay-based fault  
94 zone gouge of the Japan Trench found them to be predominantly velocity-strengthening, but  
95 with some amount of velocity-weakening and velocity-neutral behavior [17].

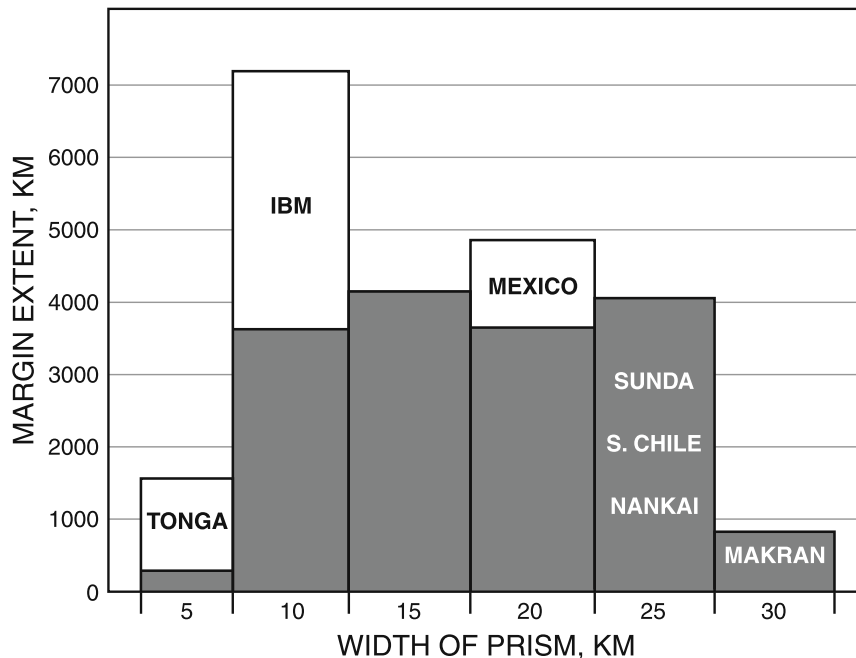


Figure 1: Histogram of prism widths in global subduction zones, compiled from seismic images of about 48% of the world’s convergent margins. Unshaded areas (e.g., Tonga) represent prisms whose widths are uncertain due to poor seismic image quality. IBM refers to the Izu-Bonin-Mariana margin. After von Huene et al. [49]

96 The Japan Trench samples were also found to have low absolute friction coefficients ( $f_0$ )  
 97 between 0.20 and 0.26 for the fault zone [17]. These were comparable to measurements from  
 98 other clay-rich subduction zone boundaries, including Nankai [24], Barbados [24], and Costa  
 99 Rica [18]. In this study, we explore focus mainly on the rate-dependence effect of friction  
 100 and not absolute friction (which we keep fixed at  $f_0 = 0.6$ , except in a set of simulations  
 101 utilizing  $f_0 = 0.2$ ), recognizing that the latter is important in determining the sensitivity of  
 102 fault shear strength to changes in effective normal stress.

103 We return our discussion now to material structure, in order to justify the range of prism  
 104 geometries and material properties to be explored in our simulations. Wide-angle seismic  
 105 reflection surveys and potential-field modeling have imaged the structure of subduction zone  
 106 boundaries in northern Japan [32, 33], Nankai [22, 34], Sunda [21, 25], Cascadia [8, 9], Chile  
 107 [27, 47], and elsewhere. From a structural perspective, convergent margins are complex,  
 108 and no simple model can explain them all. About 25 percent of the global span of major  
 109 subduction zones are accreting margins, which widen over geologic time scales as lower-plate  
 110 sediments transfer to the inner rock framework of the upper plate. Nonaccreting margins,  
 111 identified by a trench axis that moves landward and a bedrock framework that extends

112 offshore to within a few tens of kilometers of the trench, make up the other 75 percent  
113 [40]. Despite the differences in tectonic setting, geophysical data show that both accreting  
114 and nonaccreting margins have frontal prisms made up of actively deforming sedimentary  
115 material. The frontal prism is underlain by a sedimentary apron of shelf-slope deposits, which  
116 can include significant amounts of mass wasting debris [48]. Frontal prisms are typically 5–30  
117 kilometers wide and can be several kilometers thick (Figure 1) [49]. The landward boundary  
118 of a frontal prism is defined by a mechanical backstop, a transition to a little-deforming  
119 middle prism (in the case of an accreting margin) or to a section of fragmented inner prism  
120 bedrock (in a nonaccreting margin) [40]. Our simulations span the typical width range of  
121 frontal prisms and ignore structural differences between accreting and nonaccreting margins.

122 Frontal prisms are composed of sedimentary materials that are more compliant than  
123 the surrounding bedrock framework. Modeling frontal prisms accurately requires the use of  
124 realistically low values for elastic moduli and wave speeds of prism sediments. Core samples  
125 from the frontal prism of the Japan Trench provide a specific example of how compliant  
126 these sediments can be. Ultrasonic p- and s-wave velocities were measured on core samples  
127 recovered at depths ranging from 690.4 to 818.5 mbsf ( $\sim 7.6$  km below sea level). Confining  
128 (effective) pressure was elevated stepwise from 1 to 18 MPa, and measurements showed a  
129 range of p-wave velocities ( $\alpha$ ) from 1.84 to 3.29 km/s and a range of s-wave velocities ( $\beta$ ) from  
130 0.80 to 1.16 km/s. The in situ values for  $\alpha$ ,  $\beta$ , and  $\alpha/\beta$  were estimated as 2.00 to 2.48 km/s,  
131 0.89 to 1.10 km/s, and 2.05 to 2.48, respectively [33]. The corresponding values for shear  
132 modulus and bulk modulus were 1.4 to 2.2 GPa and 7.2 to 11.1 GPa, respectively, assuming  
133 an approximate in situ density of 1.8 g/cm<sup>3</sup> [4]. These results are consistent with the highly  
134 compliant material properties observed in frontal prisms in Cascadia [46], Nankai [37], Costa  
135 Rica [12], and Barbados [45]. Elastic moduli from deeper parts of the subduction zone are  
136 typically an order of magnitude or more larger. Our models span a wide range of material  
137 property values in the frontal prism, including these very compliant values.

## 138 2 Dynamic Rupture Modeling

139 We use 2D plane strain dynamic rupture models of a thrust fault intersecting the ocean  
140 in order to perform a parameter space survey of the factors that most strongly impact  
141 shallow slip and tsunamigenesis. Our numerical method [29] fully couples dynamic rupture  
142 to the elastodynamic response of the solid Earth and the ocean. Both compressibility and  
143 gravity are accounted for in the ocean, using a linearized Eulerian description to solve for  
144 perturbations about an initial hydrostatic state. Both ocean acoustic waves and tsunamis  
145 (including dispersion and nonhydrostatic effects in tsunami generation) are captured in this

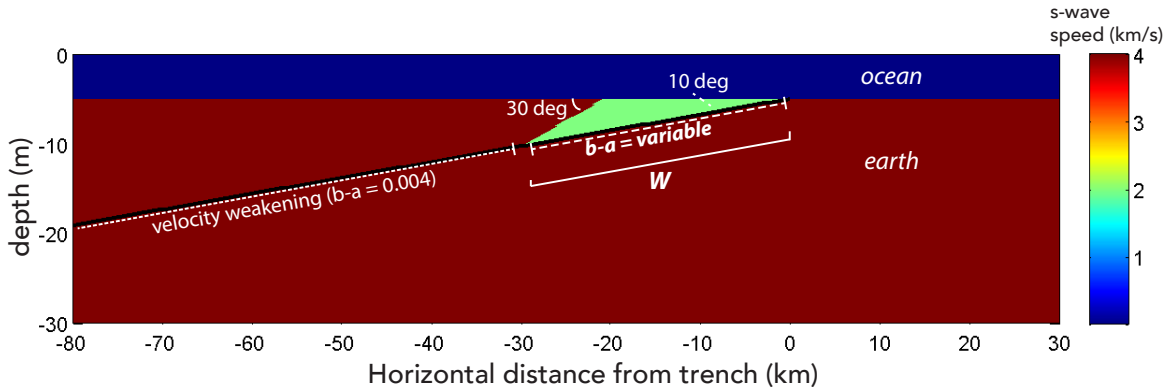


Figure 2: Geometry of the simulations in this study. A fault runs through the Earth with a  $10^\circ$  dip angle, intersecting the seafloor, which has a flat bathymetry. In this image,  $W = 30$  km and  $r$ , the ratio of the shear wave speed in the background Earth to that in the prism, is equal to 2.

146 approach. By dynamically coupling seafloor deformation to the ocean surface response, we  
 147 can study the entire tsunami generation process without relying on approximations of initial  
 148 conditions on sea surface height and depth-averaged horizontal particle velocity that are  
 149 required in the commonly used shallow water wave theory.

150 We choose a geometry for our models that is as simple as possible while including some  
 151 of the more pertinent features of subduction zone boundaries from around the world. In  
 152 our geometry (Figure 2), a 144-km-long thrust fault cuts through the Earth with a  $10^\circ$  dip  
 153 angle, intersecting the ocean bottom at the subduction trench. The seafloor is flat and  
 154 the ocean depth is 5 km. (A study of tsunami generation in the presence of a sloping  
 155 seafloor is deferred to future work.) The landward border of the prism dips at a  $30^\circ$  angle  
 156 from horizontal, typical of backstops that commonly define the edge of outer prisms in real  
 157 subduction zones [49]. In this study, we do not allow for slip on splay faults that frequently  
 158 demarcate prism backstops; all slip is confined to the plate boundary interface. The size of  
 159 the prism is determined by the parameter  $W$ , which is defined as the downdip extent of the  
 160 prism.

161 Material properties at every grid point are defined by three elastic parameters: density  
 162  $\rho$ , s-wave speed  $\beta$ , and p-wave speed  $\alpha$ . In the ocean,  $\rho_o = 1.0$  g/cm<sup>3</sup>,  $\beta_o = 0$  km/s, and  
 163  $\alpha_o = 1.5$  km/s; everywhere in the Earth except for the prism,  $\rho_e = 2.8$  g/cm<sup>3</sup>,  $\beta_e = 4.0$   
 164 km/s, and  $\alpha_e = 7.0$  km/s, consistent with lower crustal materials. To select the material  
 165 properties in the prism, we interpolate between the background values and values found in  
 166 the compliant prism of the Japan Trench at the JFAST drilling site [33], namely  $\rho_l = 2.0$   
 167 g/cm<sup>3</sup>,  $\beta_l = 0.9$  km/s, and  $\alpha_l = 2.0$  km/s. The three elastic parameters in the prism,  $\rho_p$ ,  $\beta_p$ ,

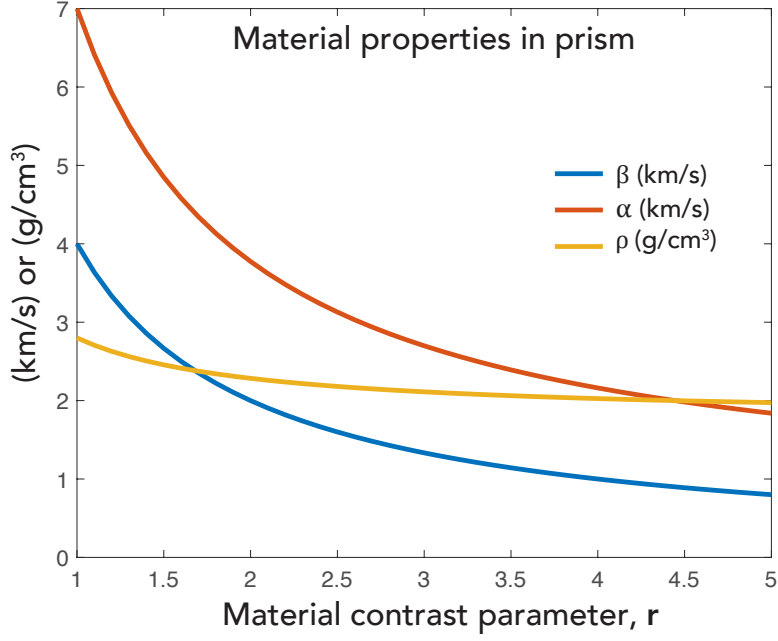


Figure 3: Dependence of  $\beta_p$ ,  $\alpha_p$ , and  $\rho_p$  on the material contrast parameter  $r$ .

168 and  $\alpha_p$ , are varied together by selecting a value for  $r$ , a dimensionless parameter defined as

$$r = \frac{\beta_e}{\beta_p}. \quad (1)$$

169 Selecting the material contrast parameter  $r$  sets a value for  $\beta_p$ , and then  $\rho_p$  and  $\alpha_p$  are  
 170 calculated by interpolating between the background values in the Earth and those in the  
 171 Japan trench. For example,  $\rho_p$  is calculated as

$$\rho_p = \rho_l + (\rho_e - \rho_l) \frac{(1 - \beta_l/\beta_p)}{(r - \beta_l/\beta_p)} \quad (2)$$

172 and  $\alpha_p$  is calculated similarly (Figure 3). By selecting different values of  $r$ , we sweep through  
 173 not only parameters but also ratios of parameters, including  $\alpha/\beta$ , which ratio is 1.75 in the  
 174 background rock and 2.22 in the Japan Trench. We also mention that while the present study  
 175 is limited to the elastic response of off-fault materials, prism sediments are also weak in terms  
 176 of their susceptibility to inelastic deformation, which may impact the rupture process in real  
 177 subduction zones [31].

178 Rupture on the fault is governed by the rate-and-state friction law in a differential form  
 179 [26]:

$$\frac{d\tau}{dt} = \frac{a\bar{\sigma}}{V} \tanh\left(\frac{\tau}{a\bar{\sigma}}\right) \frac{dV}{dt} - \frac{V}{l} [|\tau| - \bar{\sigma}f_{ss}(V)], \quad (3)$$

180 with the steady-state friction coefficient given by

$$f_{ss}(V) = f_0 - (b - a) \ln(V/V_0), \quad (4)$$

181 where  $\tau$  is the shear strength of the fault,  $\bar{\sigma}$  is the effective normal stress,  $V$  is the slip  
182 velocity,  $l = 0.8$  m is the state evolution distance,  $V_0 = 1$   $\mu\text{m/s}$  is the reference velocity,  
183 and  $b$  and  $a$  are dimensionless parameters. For positive  $b - a$ , increases in  $V$  decrease steady  
184 state friction  $f_{ss}$ , leading to potentially unstable slip and earthquake nucleation. For negative  
185  $b - a$ , increasing  $V$  increases  $f_{ss}$ , inhibiting unstable slip. In our models, we apply velocity  
186 weakening ( $b - a = 0.004$ ) friction everywhere except in the region beneath the prism. On  
187 the shallow fault segment defined by  $W$ , we vary  $b$  so that the fault ranges from velocity  
188 weakening properties ( $b - a = 0.004$ ) to velocity strengthening properties ( $b - a = -0.004$ ).  
189 The friction law (4) does not let shear stress instantaneously respond to changes in effective  
190 normal stress. This avoids ill-posedness that can occur in bimaterial slip problems for friction  
191 laws in which  $\tau$  is directly proportional to the instantaneous value of  $\bar{\sigma}$ .

192 We set  $f_0$ , the friction coefficient for steady sliding at  $V_0$ , to a constant  $f_0 = 0.6$ , despite  
193 some evidence (cited above) that absolute friction may be lower in clay-rich subduction  
194 zones. Though the effects of varying absolute fault friction are largely out of the scope of  
195 this paper, the simulations we ran using  $f_0 = 0.2$  show somewhat lower slip at the trench but  
196 qualitatively similar results as when  $f_0 = 0.6$  (see Supplementary Figure 1). The decreased  
197 slip at the trench is due to the fact that initial shear stress must be set lower when the absolute  
198 friction coefficient is lower. Differences between  $f_0 = 0.6$  and  $f_0 = 0.2$  are more pronounced  
199 in models with velocity-weakening friction and more compliant prisms, i.e., models with  
200 higher slip at the trench.

201 In order to account for poroelastic changes in pore pressure,  $\Delta p$ , as a response to changes  
202 in total normal stress,  $\Delta\sigma$ , we use the linear relation  $\Delta p = B\Delta\sigma$ , with  $B = 0.6$ . The  
203 poroelastic effect alters stress as

$$\bar{\sigma} = \bar{\sigma}_0 + (1 - B)\Delta\sigma, \quad (5)$$

204 which serves to partially buffer the changes in effective normal stress. Equation 5 is a limiting  
205 case of a model [6] where the fault is surrounded by highly damaged material; in that limit,  
206  $B$  is Skempton's coefficient.

207 Initial effective normal stress  $\bar{\sigma}_0$  is calculated as the difference between normal stress  
208 in the Earth and pore pressure. Normal stress on the fault is set to lithostatic – a decent  
209 approximation given the shallow fault dip – and pore pressure is hydrostatic. Effective normal  
210 stress increases with depth to a maximum of  $\bar{\sigma}_0 = 40$  MPa, at which point pore pressure

211 increases lithostatically. Initial shear stress on the fault,  $\tau_0$ , is  $\tau_0 = 0.6\bar{\sigma}_0$ . Earthquakes are  
212 nucleated by perturbing shear stress on the fault at a depth of 13 km below the seafloor, 75  
213 km away from the trench.

214 We perform a parameter space survey in three dimensions:  $r$ ,  $W$ , and  $b - a$  at the base  
215 of the prism. The values we use are  $r = 1, 2, 3, 4, 5$ ;  $W = 10, 20, 30$  km; and  $b - a =$   
216  $0.004, 0.002, 0.000, -0.002, -0.004$ .

217 For most simulations, we use a grid spacing of 200 m in both the vertical and horizontal  
218 directions. For the majority of our simulations, mesh refinement leads to little or no difference  
219 (less than  $\sim 2\%$ ) in final slip and tsunami height. However, at the edge of parameter space  
220 where  $W = 30$  km and  $b - a = \pm 0.004$ , doubling the mesh resolution leads to a more  
221 substantial (greater than  $\sim 5\%$ ) change in slip. In those cases (i.e., Figure 7a-b,i-j), we show  
222 the results of simulations with 100 m grid spacing.

### 223 3 Results and Discussion

224 The parameter space survey reveals that prism size, compliance, and friction each help  
225 determine fault slip and tsunami height, and that the parameters  $r$ ,  $W$ , and  $b - a$  interact  
226 with each other in significant and sometimes unexpected ways. Most notably, we find that  
227 in most but not all cases, the presence of a compliant prism causes enhanced slip which in  
228 turn increases tsunami heights. However, compliant prisms also play several other roles in  
229 the earthquake rupture process.

230 For example, we find that for prisms of all sizes, the rupture velocity slows significantly  
231 as rupture reaches the prism, due to lower shear speeds (Figure 4). Sub-prism friction  
232 can influence rupture velocity by inducing supershear propagation at the base of the prism  
233 when friction is velocity-weakening (compare Figure 4c and d). Models with  $r = 1$ , i.e.,  
234 no material property contrast between the prism and surrounding rock, have sub-Rayleigh  
235 rupture velocities that are fairly constant with depth or speed up slightly near the trench  
236 (Figure 4a and b). Note that simulations with  $r = 1$  have no compliant prism, but they  
237 do have frictional properties determined by  $W$  and  $b - a$ ; this accounts for the difference in  
238 results between Figure 4a and b.

239 However, earthquakes that rupture through compliant prisms slow considerably as they  
240 approach the trench, limited by the shear-wave speed in the prism (Figure 4c and d). Note  
241 that even though  $r$  largely controls the rupture velocity, slip velocity and total slip are  
242 strongly influenced by shallow friction. For example, comparing Figure 4c and d we see that  
243 in both cases rupture velocity slows in the 30-km region at the base of the prism due to  
244 the compliant material properties within the prism. But only in d, the simulation where

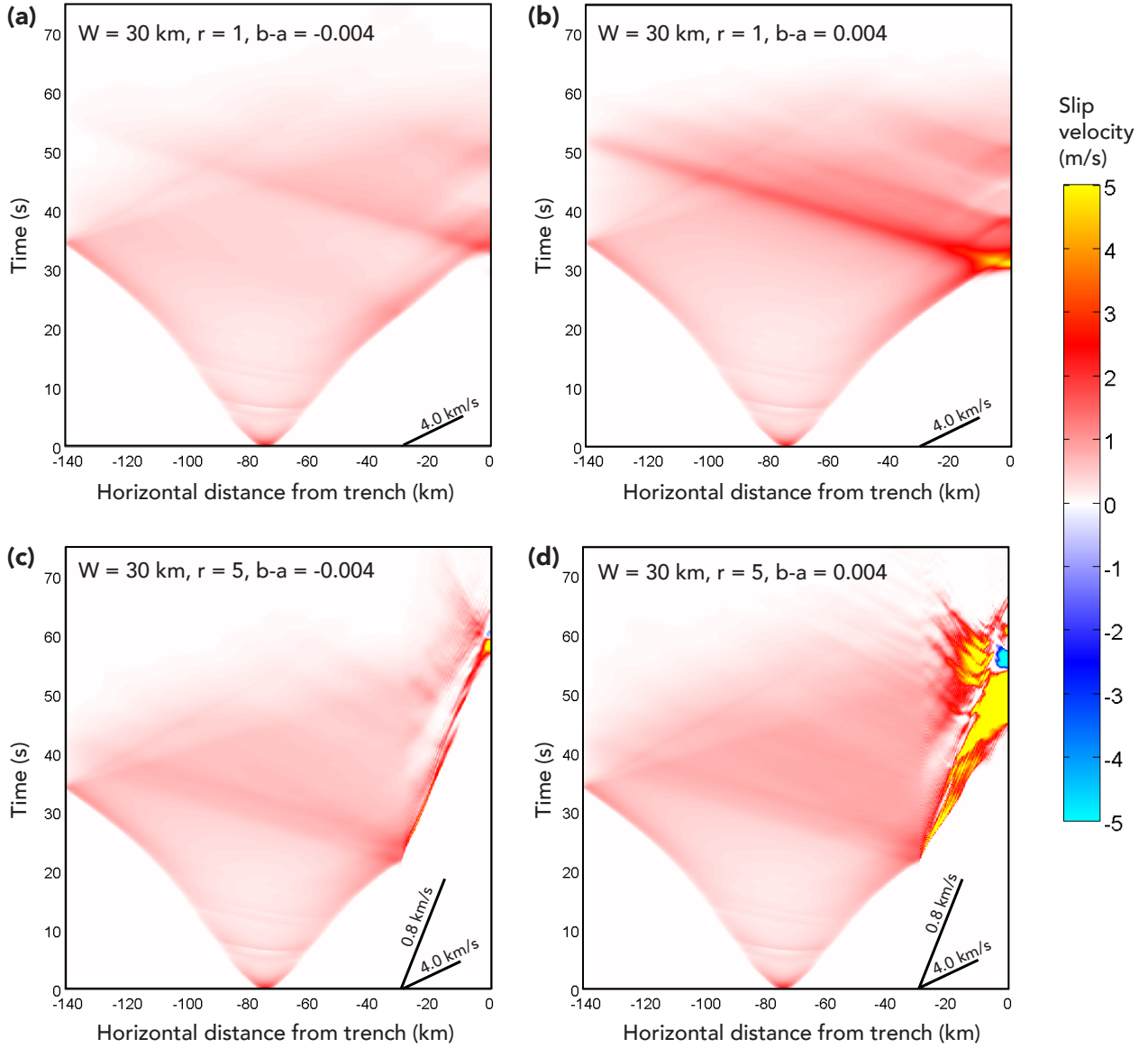


Figure 4: Time-space plots of slip velocity for four different simulations, all with  $W = 30$  km. Dark black lines are drawn at the representative shear wave speeds in the medium,  $4.0$  km/s where there is no prism and  $0.8$  km/s in the prism in simulations where  $r = 5$ . (a)  $r = 1$ ,  $b - a = -0.004$  beneath the prism. Rupture velocity is consistent at all depths along the fault. (b)  $r = 1$ ,  $b - a = 0.004$  beneath the prism. Rupture velocity is consistent at all depths, but slip velocity increases due to velocity-weakening friction. (c)  $r = 5$ ,  $b - a = -0.004$  beneath the prism. Rupture slows appreciably on the fault at the base of the prism due to highly compliant material properties. (d)  $r = 5$ ,  $b - a = 0.004$  beneath the prism. Rupture slows appreciably but slip velocity is greatly enhanced.

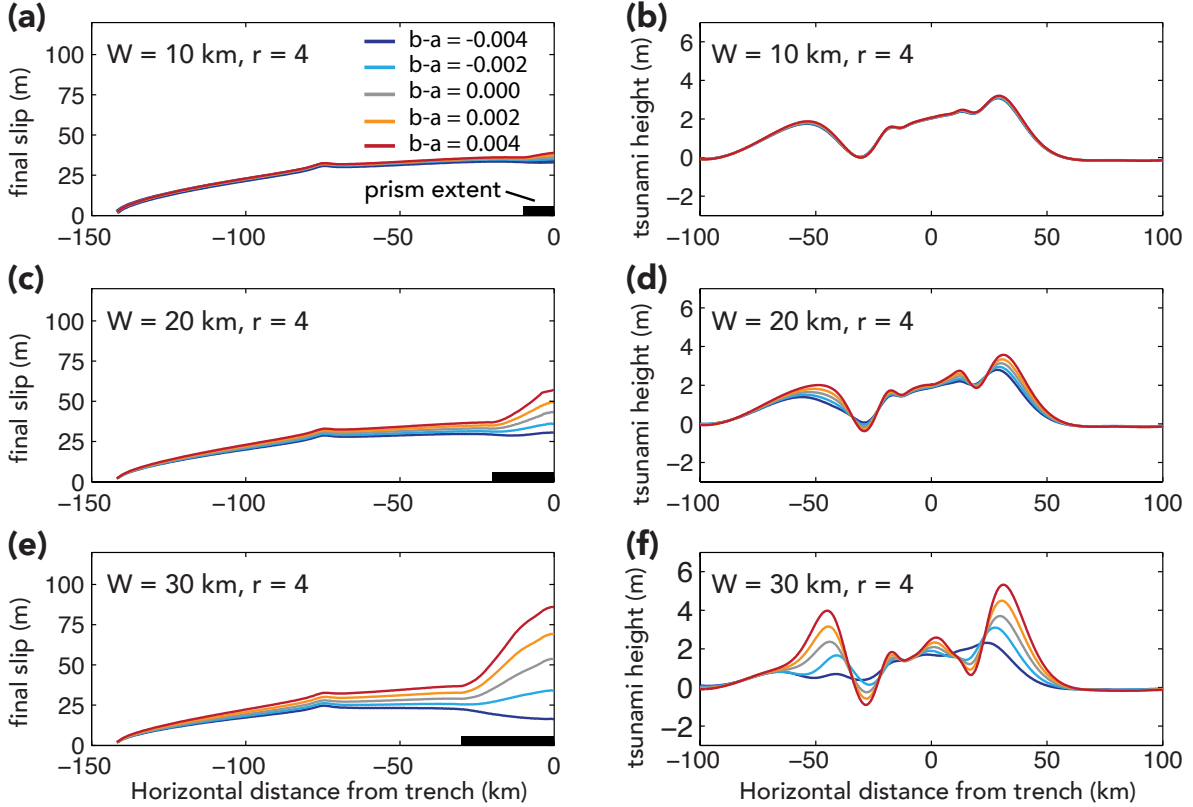


Figure 5: Total slip and tsunami height (vertical displacement at the sea surface) for simulations with  $r = 4$ , plotted at time  $t = 250$  s. In each plot,  $W$  is held fixed and friction is varied as  $b - a = -0.004, -0.002, 0, 0.002, 0.004$ . (a) and (b):  $W = 10$  km and changing shallow friction has little effect on slip and tsunami height. (c) and (d):  $W = 20$  km and changing shallow friction has a moderate effect on slip and tsunami height. (e) and (f):  $W = 30$  km and changing shallow friction has a great effect on slip and tsunami height.

245 sub-prism friction is velocity weakening, does slip velocity notably increase.

246 We present a series of simulations holding  $W$  and  $r$  constant while varying shallow  $b - a$ .  
 247 We find that moving from velocity-strengthening to velocity-weakening friction – increasing  
 248 the parameter  $b - a$  – on the fault at the base of the prism resulted in greater amounts of  
 249 slip, not only near the trench but also deeper down along the fault (e.g., Figure 5). The  
 250 reason for this enhanced slip along the entire fault can be seen by comparing Figure 4a and  
 251 b; when the fault is velocity-weakening at the trench (as in b), the rupture propagates back  
 252 down the fault after reaching the trench. Increasing  $b - a$ , i.e., enhancing slip, also leads to  
 253 the generation of larger tsunamis. Tsunami height is defined herein as vertical displacement  
 254 at the sea surface at time  $t = 250$  s, by which point all ocean acoustic waves have propagated  
 255 out of the domain. The time of measurement is somewhat arbitrarily chosen, but since our  
 256 simulations are in 2-D, there is no amplitude decay from geometric spreading and only a

257 slight amount from dispersion. The effects of modifying  $b - a$  are more pronounced for larger  
258 prisms than for smaller prisms (Figure 5), and in this sense we can view prism size  $W$  as  
259 having an amplifying effect on enhanced slip and tsunamigenesis.

260 Separately, we look at a series of simulations where we hold  $W$  and  $b - a$  constant and vary  
261 the prism compliance,  $r$ . The results of these simulations turn out to be highly dependent  
262 on the choice of  $b - a$ . For example, when  $b - a \geq -0.002$ , increasing the compliance of  
263 the prism leads to greatly enhanced slip and significantly larger tsunamis (see Figure 6a-j  
264 and Figure 7c-j). This phenomenon is true for prisms of any considerable size. That more  
265 compliant prisms tend to enhance shallow slip and tsunamigenesis for most choices of shallow  
266  $b - a$  and  $W$  is unsurprising, given the general consensus in the tsunami community that  
267 compliant sedimentary material is often associated with tsunami earthquakes (e.g., [20,36]).

268  
269 However, we find that in certain circumstances increasing  $r$  actually leads to decreased  
270 slip. In particular, when  $W = 30$  km and  $b - a = -0.004$  (velocity-strengthening shallow  
271 friction), prism compliance is negatively correlated with shallow slip (Figure 7a). This is an  
272 unintuitive result given the role compliant prisms are generally thought to play in enhancing  
273 tsunamigenesis via shallow deformation. We have found no clear explanation for this result,  
274 but we offer some observations from slip history plots (see Supplementary Figure 2). When  
275  $W = 30$  km and  $b - a = -0.004$ , the simulation with no compliant prism ( $r = 1$ ) results in  
276 a rupture that propagates smoothly through the region with velocity-strengthening friction.  
277 But with a compliant prism ( $r = 3$  and  $r = 5$ ), the rupture slows significantly in the prism  
278 and partially reflects, propagating back down the fault. Meanwhile, the upward-propagating  
279 rupture front decreases in slip velocity and barely makes it all the way through to the trench.  
280 The most obvious difference between models with and without a compliant prism is that with  
281 a compliant prism, slip velocity goes nearly to zero below the rupture front as the rupture  
282 propagates through the prism. By the time the rupture reaches the trench, there is a deficit  
283 of slip in the shallow part of the fault that is never overcome.

284 We note that for low values of  $r$ , slip is nearly uniform in the shallow portion of the fault,  
285 only a few meters higher at the trench than at depth (see, e.g., the grey curve in Figure 6i).  
286 This result might, at first, seem to conflict with Geist and Dmowska [11], who found, in  
287 their study of static elastic solutions for constant stress drop cracks on dipping faults, that  
288 slip should take its maximum value at the free surface. However, in our simulations stress  
289 drop is not constant on the fault but rather decreases toward the trench, which may account  
290 for some of the difference. Additionally, our simulations include inertia whereas Geist and  
291 Dmowska calculated a static displacement field from an ideal crack model.

292 Across our simulations, there is no straightforward linear relation between compliance

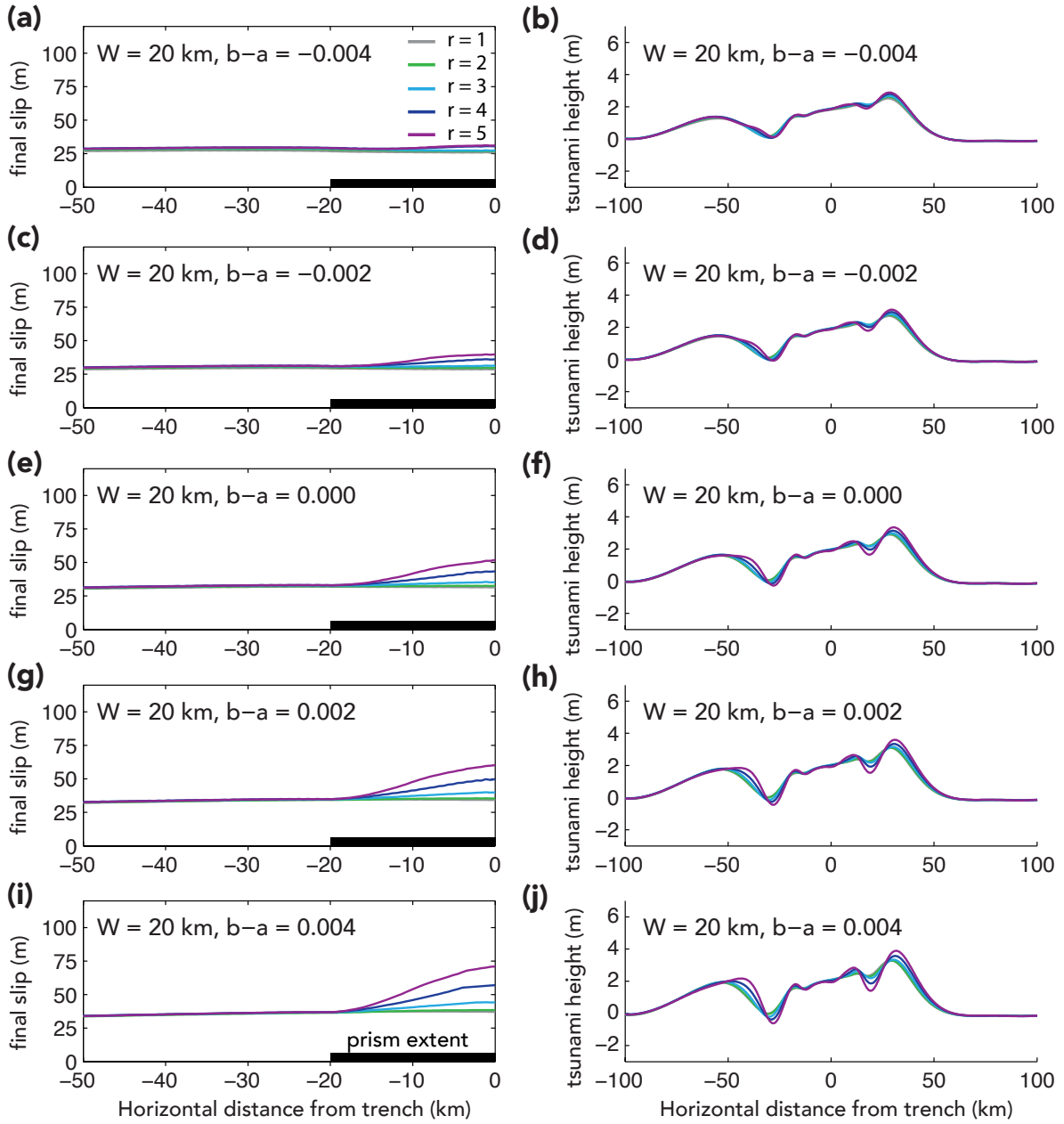


Figure 6: Total slip and tsunami height for simulations with  $W = 20$  km, plotted at time  $t = 250$  s. In each plot,  $b - a$  is held fixed and prism compliance is varied as  $r = 1, 2, 3, 4, 5$ . For prisms of width  $W = 20$  km and smaller, increases in prism compliance always lead to more slip and greater amplitude tsunamis, independent of shallow  $b - a$ . Downtip of the prism, slip is nearly equivalent for all simulations with the same value of  $b - a$ .

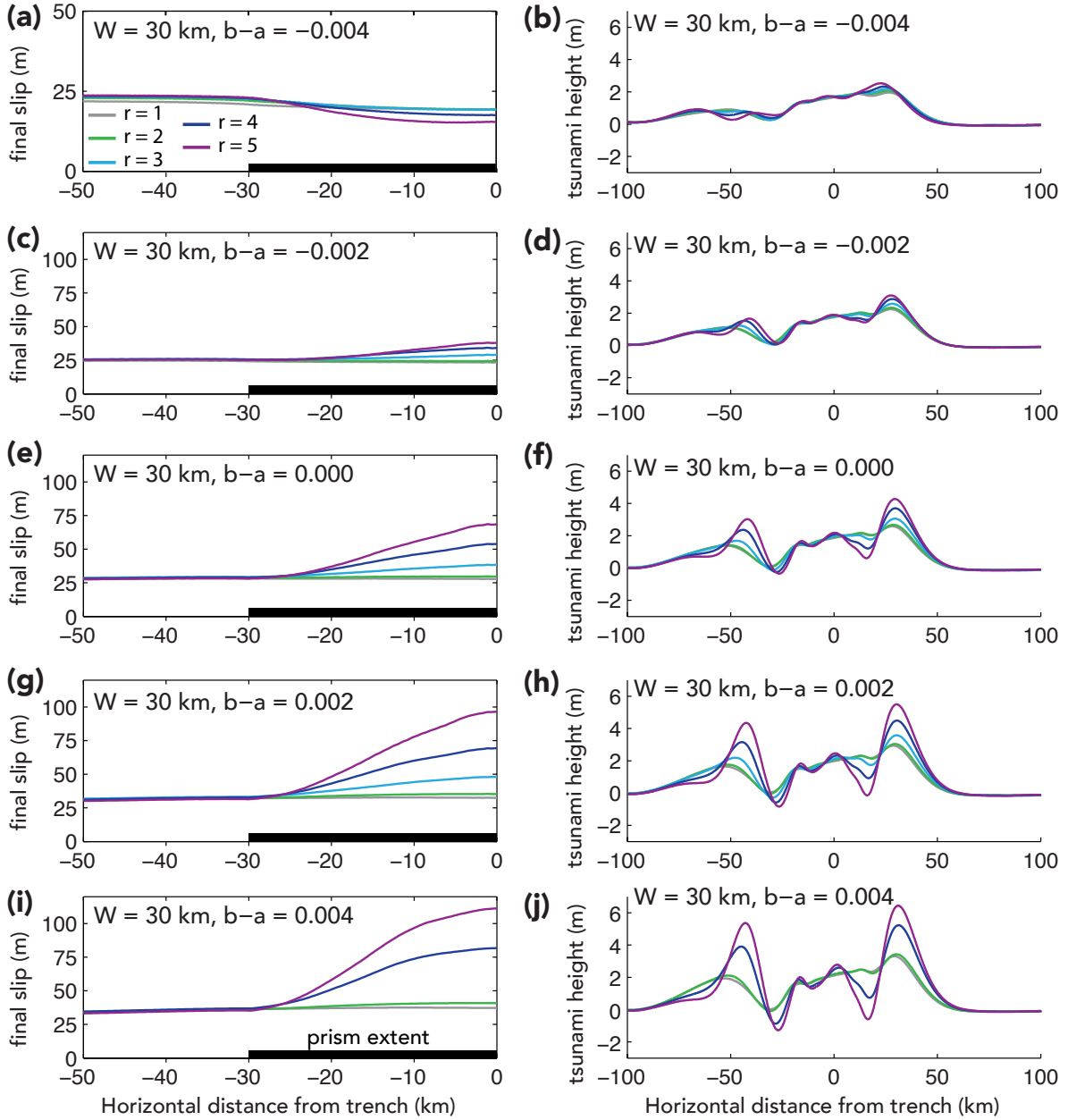


Figure 7: Total slip and tsunami height for simulations with  $W = 30$  km, plotted at time  $t = 250$  s. In each plot,  $b - a$  is held fixed and prism compliance is varied as  $r = 1, 2, 3, 4, 5$ . For larger prisms ( $W = 30$  km), increases in prism compliance sometimes lead to more slip and greater amplitude tsunamis, for example when  $b - a \geq -0.002$  ( (c)–(j) ). However, when  $b - a = -0.004$ , more compliant prisms actually experience less slip ( (a) and (b) ). In (a), the vertical axis is compressed for emphasis. Downtip of the prism, slip is nearly equivalent for all simulations with the same value of  $b - a$ .

293 and shallow slip as might have been anticipated from linear elasticity in a homogeneous  
 294 medium. For example, in Figure 6(i), when  $r = 2$  the ratio of the shear modulus in the  
 295 surrounding Earth to that in the prism is  $44.8 \text{ GPa}/9.1 \text{ GPa} \approx 4.9$ , but the shallow slip is  
 296 nearly identical to the  $r = 1$  case. Only when that ratio gets much more extreme – 11.9 for  
 297  $r = 3$ , 22.1 for  $r = 4$ , 35.5 for  $r = 5$  – does slip increase significantly.

298 We can quantify the time-dependent earthquake source process using seismic potency  
 299 per distance along strike,  $P$ , defined as

$$P(t) = \int_{-L}^0 s(x, t) dx, \quad (6)$$

300 where  $s$  is slip and  $x$  follows the downdip axis over fault length  $L = 144 \text{ km}$ . Potency  
 301 is equivalent to moment per unit rigidity, and avoids any ambiguities in choosing a shear  
 302 modulus when, for instance, there are different materials on opposite sides of the fault. We  
 303 also define potency rate,  $\dot{P} = dP/dt$ . In Figure 8, we plot  $\dot{P}$  as a function of time for various  
 304 simulations with  $W = 30 \text{ km}$ , which lets us observe differences in slip history for different  
 305 sets of parameters. For  $b - a \geq -0.002$ , we see a peak in potency rate that is dependent  
 306 on prism compliance, where more compliant prisms see a delayed peak in  $\dot{P}$  due to rupture  
 307 velocity decreasing with larger  $r$ . Naturally, this peak in  $\dot{P}$  is greater for higher values of  
 308  $b - a$ . For the case where  $b - a = -0.004$ , the correlation between  $r$  and the time of peak  $\dot{P}$  is  
 309 less clear, especially for the most compliant model. For  $r = 5$ , the rupture slows significantly  
 310 but does not generate enough shallow slip to appear as a peak in potency rate.

311 Finally, in order to get a measure of an earthquake’s efficiency at generating tsunamis,  
 312 we define the dimensionless quantity  $\varepsilon$  as

$$\varepsilon = \frac{h_{max}}{P/L} = \frac{h_{max}}{\langle s \rangle}, \quad (7)$$

313 where  $h_{max}$  is the maximum tsunami height at a given time. We note that  $P/L$  is the average  
 314 slip on the fault,  $\langle s \rangle$ . Tsunami efficiency,  $\varepsilon$ , is measured at time  $t = 250 \text{ s}$ , at which point all  
 315 higher-frequency acoustic waves oscillating in the compressible ocean have propagated out  
 316 of the domain. A larger value of  $\varepsilon$  indicates that for a given set of parameters, the resulting  
 317 tsunami is large relative to the amount of slip along the entire fault. Figure 9 shows that  
 318 in medium and large prisms ( $W = 20, 30 \text{ km}$ ), tsunami efficiency increases with  $r$  and with  
 319 shallow  $b - a$ . In smaller prisms ( $W = 10 \text{ km}$ ),  $\varepsilon$  has a small but negative correlation with  
 320  $r$ . Small compliant prisms cause increased slip at the trench but slightly decreased slip at  
 321 depth, leading to average slip that is about equivalent to models with no compliant prism.  
 322 This slip pattern actually leads to very slightly lower maximum tsunami heights, and thus

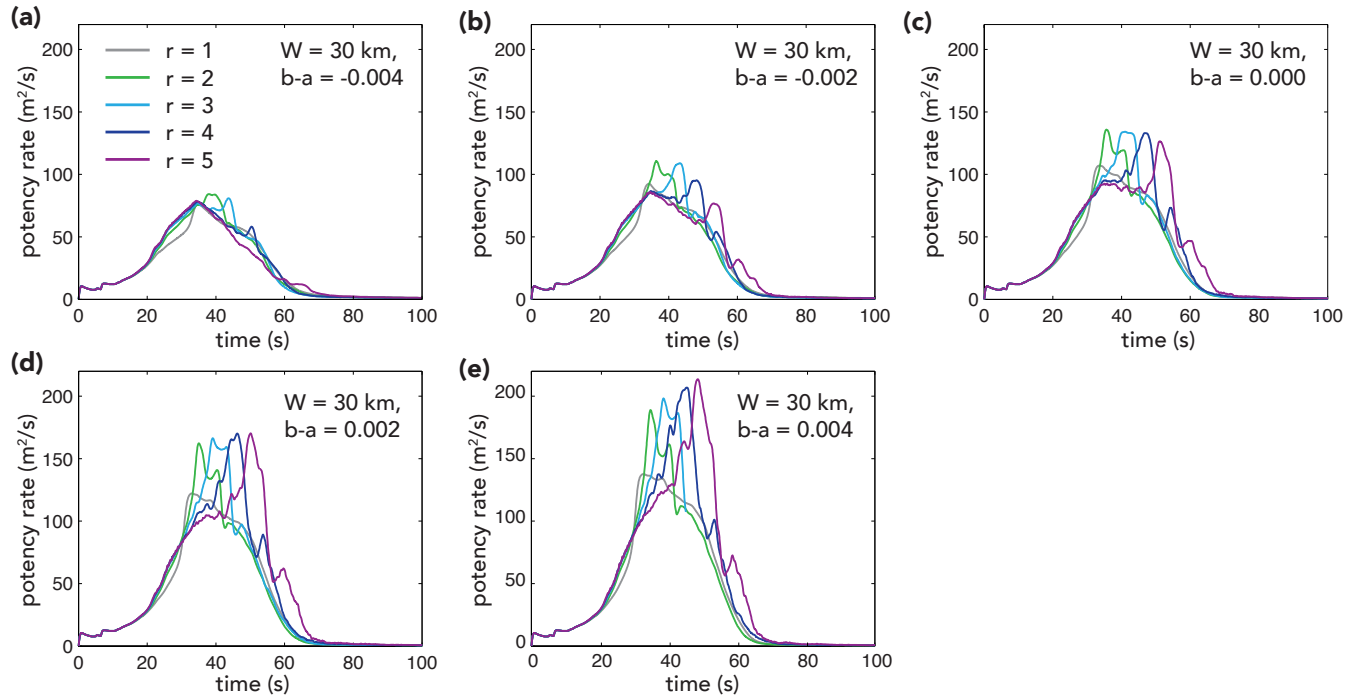


Figure 8: Potency rate  $\dot{P}$  for  $W = 30$  km. For  $b - a \geq -0.002$ , more compliant prisms lead to later peaks in  $\dot{P}$ . This phenomenon is less clear when  $b - a = -0.004$ .

323 a decreased  $\varepsilon$ .

## 324 4 Conclusions

325 Earthquakes that rupture through compliant prisms can exhibit many of the characteristics  
 326 of tsunami earthquakes. On the fault at the base of the prism, rupture velocity slows sig-  
 327 nificantly, limited by the lower shear wave speed of prism sediments. Shallow slip usually  
 328 increases compared to models without a prism, enhancing seafloor deformation and creating  
 329 larger tsunamis. With larger and more compliant prisms and more favorable frictional condi-  
 330 tions, these earthquakes can generate tsunamis very efficiently with respect to the total slip  
 331 they produce. Smaller compliant prisms tend to have little to no effect on tsunami height,  
 332 regardless of friction and material properties.

333 Figure 10 summarizes the effects of the material contrast parameter  $r$ , prism size  $W$ ,  
 334 and shallow rate-and-state friction parameter  $b - a$  on the rupture process. In most parts  
 335 of parameter space, increasing prism compliance  $r$  leads to enhanced shallow slip and larger  
 336 tsunamis. However, in simulations with velocity-strengthening friction ( $b - a = -0.004$ ) and  
 337 a large prism ( $W = 30$  km), the presence of a more compliant prism reduces shallow slip.

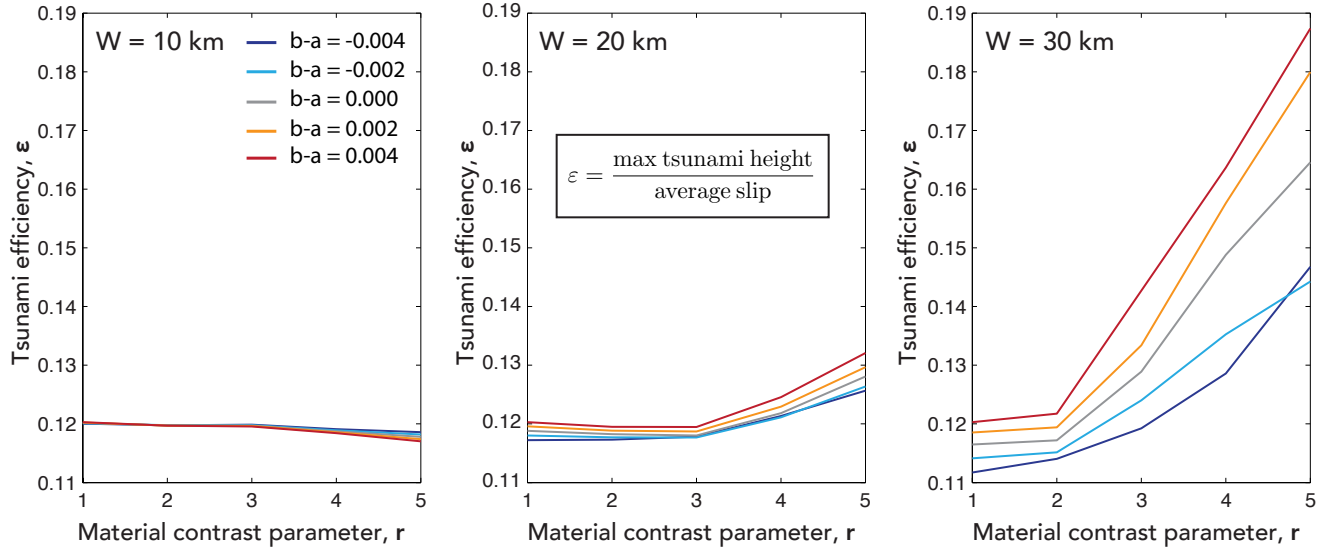


Figure 9: Tsunami efficiency, defined as the ratio of maximum tsunami height (at time  $t = 250$  s) to average slip. Earthquakes that rupture through medium and large prisms more efficiently generate tsunamis when  $b - a$  and  $r$  are larger.

338 Increasing the rate-and-state parameter  $b - a$  at the base of the prism leads to increased slip  
 339 not only beneath the prism but also deeper down along the entire fault. Increasing the size  
 340 of the prism,  $W$ , tends to amplify the effects of changing  $r$  and  $b - a$ .

341 The wide range of results produced by varying just these three parameters points to the  
 342 importance of studying subduction zone earthquakes with realistically complex numerical  
 343 models, and of continuing to gather data on frictional and material properties of prisms in  
 344 convergent margins where tsunamis may pose a significant threat to local populations.

## 345 References

- 346 [1] Charles J Ammon, Hiroo Kanamori, Thorne Lay, and Aaron A Velasco. The 17 July  
 347 2006 Java tsunami earthquake. *Geophysical Research Letters*, 33(24), 2006.
- 348 [2] David J Andrews and Yehuda Ben-Zion. Wrinkle-like slip pulse on a fault between  
 349 different materials. *Journal of Geophysical Research*, 102:553–571, 1997.
- 350 [3] Susan L Bilek and Thorne Lay. Tsunami earthquakes possibly widespread manifesta-  
 351 tions of frictional conditional stability. *Geophysical Research Letters*, 29(14), 2002.
- 352 [4] Frederick M Chester, Junichiro Mori, Nawo Eguchi, and Sean Toczko. Expedition  
 353 343/343t scientists: Site c0019. Technical report, The Expedition 343/343T Scientists,

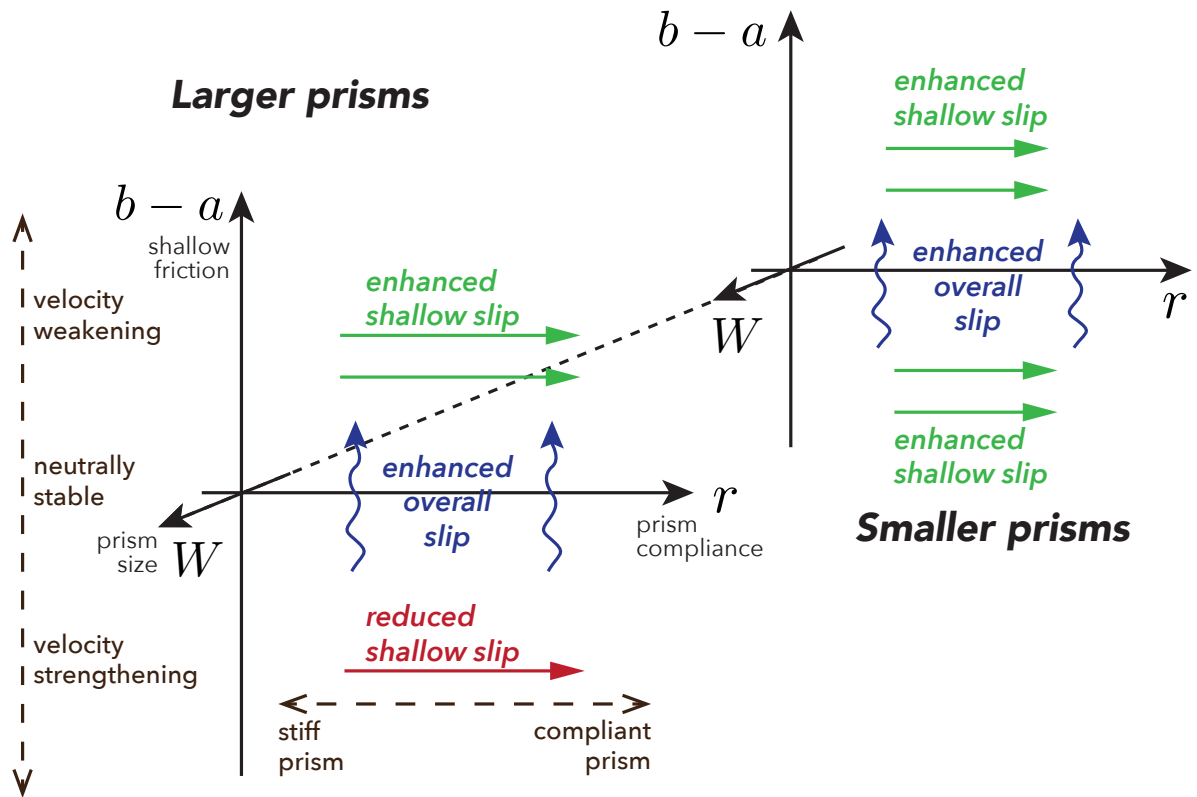


Figure 10: Schematic of parameter space and the effects of  $r$ ,  $W$ , and  $b - a$  on fault slip. For larger prisms, increasing  $r$  leads to enhanced shallow slip when  $b - a$  is positive, but leads to reduced shallow slip when  $b - a$  is negative. For smaller prisms, increases in  $r$  always result in more shallow slip. Increasing  $b - a$  enhances slip on all parts of the fault. Increasing  $W$  amplifies the effects of  $r$  and  $b - a$ .

- 354 Proc. IODP, 343/343T. Integrated Ocean Drilling Program Management International,  
355 Inc, Tokyo, 10.2204/iodp.proc.343343T.103.2013, 2013.
- 356 [5] Mohamed Chlieh, Jean-Philippe Avouac, Vala Hjorleifsdottir, Teh-Ru Alex Song, Chen  
357 Ji, Kerry Sieh, Anthony Sladen, Helene Hebert, Linette Prawirodirdjo, Yehuda Bock,  
358 et al. Coseismic slip and afterslip of the great Mw 9.15 Sumatra–Andaman earthquake  
359 of 2004. *Bulletin of the Seismological Society of America*, 97(1A):S152–S173, 2007.
- 360 [6] Massimo Cocco and James R Rice. Pore pressure and poroelasticity effects in Coulomb  
361 stress analysis of earthquake interactions. *Journal of Geophysical Research: Solid Earth*,  
362 107(B2), 2002.
- 363 [7] Sabine A M den Hartog and Christopher J Spiers. Influence of subduction zone condi-  
364 tions and gouge composition on frictional slip stability of megathrust faults. *Tectono-*  
365 *physics*, 600:75–90, 2013.
- 366 [8] Sean W Fleming and Anne M Tréhu. Crustal structure beneath the central Oregon  
367 convergent margin from potential-field modeling: Evidence for a buried basement ridge  
368 in local contact with a seaward dipping backstop. *Journal of Geophysical Research:*  
369 *Solid Earth*, 104(B9):20431–20447, 1999.
- 370 [9] Ernst R Flueh, Michael A Fisher, Joerg Bialas, Jonathan R Childs, Dirk Klaeschen,  
371 Nina Kukowski, Tom Parsons, David W Scholl, Uri ten Brink, Anne M Tréhu, et al.  
372 New seismic images of the Cascadia subduction zone from cruise SO108—ORWELL.  
373 *Tectonophysics*, 293(1):69–84, 1998.
- 374 [10] Toshiya Fujiwara, Shuichi Kodaira, Yuka Kaiho, Narumi Takahashi, and Yoshiyuki  
375 Kaneda. The 2011 Tohoku-Oki earthquake: Displacement reaching the trench axis.  
376 *Science*, 334(6060):1240–1240, 2011.
- 377 [11] Eric L Geist and Renata Dmowska. Local tsunamis and distributed slip at the source. In  
378 *Seismogenic and Tsunamigenic Processes in Shallow Subduction Zones*, pages 485–512.  
379 Springer, 1999.
- 380 [12] G L Gettemy and Harold J Tobin. Tectonic signatures in centimeter-scale velocity-  
381 porosity relationships of Costa Rica convergent margin sediments. *Journal of Geophys-*  
382 *ical Research: Solid Earth*, 108(B10), 2003.
- 383 [13] Sean PS Gulick, James A Austin Jr, Lisa C McNeill, Nathan LB Bangs, Kylara M  
384 Martin, Timothy J Henstock, Jonathan M Bull, Simon Dean, Yusuf S Djajadihardja,

- 385 and Haryadi Permana. Updip rupture of the 2004 Sumatra earthquake extended by  
386 thick indurated sediments. *Nature Geoscience*, 4(7):453–456, 2011.
- 387 [14] John Hower, Eric V Eslinger, Mark E Hower, and Edward A Perry. Mechanism of  
388 burial metamorphism of argillaceous sediment: 1. Mineralogical and chemical evidence.  
389 *Geological Society of America Bulletin*, 87(5):725–737, 1976.
- 390 [15] Judith Hubbard, Sylvain Barbot, Emma M Hill, and Paul Tapponnier. Coseismic slip on  
391 shallow décollement megathrusts: implications for seismic and tsunami hazard. *Earth-*  
392 *Science Reviews*, 141:45–55, 2015.
- 393 [16] Roy D Hyndman, Makoto Yamano, and Dan A Oleskevich. The seismogenic zone of  
394 subduction thrust faults. *Island Arc*, 6(3):244–260, 1997.
- 395 [17] Matt J Ikari, Jun Kameda, Demian M Saffer, and Achim J Kopf. Strength character-  
396 istics of Japan Trench borehole samples in the high-slip region of the 2011 Tohoku-Oki  
397 earthquake. *Earth and Planetary Science Letters*, 412:35–41, 2015.
- 398 [18] Matt J Ikari, André R Niemeijer, Christopher J Spiers, Achim J Kopf, and Demian M  
399 Saffer. Experimental evidence linking slip instability with seafloor lithology and topog-  
400 raphy at the Costa Rica convergent margin. *Geology*, 41(8):891–894, 2013.
- 401 [19] Hiroo Kanamori. Mechanism of tsunami earthquakes. *Physics of the Earth and Plane-*  
402 *tary Interiors*, 6(5):346–359, 1972.
- 403 [20] Hiroo Kanamori and Masayuki Kikuchi. The 1992 Nicaragua earthquake: a slow  
404 tsunami earthquake associated with subducted sediments. *Nature*, 361(6414):714–716,  
405 1993.
- 406 [21] Frauke Klingelhoefer, M-A Gutscher, S Ladage, J-X Dessa, David Graindorge, D Franke,  
407 Camille André, Haryadi Permana, T Yudistira, and Ajay Chauhan. Limits of the seis-  
408 mogenic zone in the epicentral region of the 26 December 2004 great Sumatra-Andaman  
409 earthquake: Results from seismic refraction and wide-angle reflection surveys and ther-  
410 mal modeling. *Journal of Geophysical Research: Solid Earth*, 115(B1), 2010.
- 411 [22] Shuichi Kodaira, Eiji Kurashimo, J-O Park, Narumi Takahashi, Ayako Nakanishi, Sei-  
412 ichi Miura, Takaya Iwasaki, Naoshi Hirata, Kiyoshi Ito, and Yoshiyuki Kaneda. Struc-  
413 tural factors controlling the rupture process of a megathrust earthquake at the Nankai  
414 trough seismogenic zone. *Geophysical Journal International*, 149(3):815–835, 2002.

- 415 [23] Shuichi Kodaira, Tetsuo No, Yasuyuki Nakamura, Toshiya Fujiwara, Yuka Kaiho, Sei-  
416 ichi Miura, Narumi Takahashi, Yoshiyuki Kaneda, and Asahiko Taira. Coseismic fault  
417 rupture at the trench axis during the 2011 Tohoku-Oki earthquake. *Nature Geoscience*,  
418 5(9):646–650, 2012.
- 419 [24] Achim J Kopf and Kevin M Brown. Friction experiments on saturated sediments and  
420 their implications for the stress state of the Nankai and Barbados subduction thrusts.  
421 *Marine Geology*, 202(3):193–210, 2003.
- 422 [25] Heidrun Kopp and Nina Kukowski. Backstop geometry and accretionary mechanics of  
423 the Sunda margin. *Tectonics*, 22(6), 2003.
- 424 [26] Jeremy E. Kozdon and Eric M. Dunham. Rupture to the trench: Dynamic rupture simu-  
425 lations of the 11 March 2011 Tohoku earthquake. *Bull. Seism. Soc. Am.*, 103(2B):1275–  
426 1289, 2013.
- 427 [27] Anne Krabbenhöft, Jörg Bialas, Heidrun Kopp, Nina Kukowski, and C Hübscher.  
428 Crustal structure of the Peruvian continental margin from wide-angle seismic studies.  
429 *Geophysical Journal International*, 159(2):749–764, 2004.
- 430 [28] Thorne Lay, Charles J Ammon, Hiroo Kanamori, Yoshiki Yamazaki, Kwok Fai Cheung,  
431 and Alexander R Hutko. The 25 October 2010 Mentawai tsunami earthquake (Mw  
432 7.8) and the tsunami hazard presented by shallow megathrust ruptures. *Geophysical*  
433 *Research Letters*, 38(6), 2011.
- 434 [29] Gabriel C Lotto and Eric M Dunham. High-order finite difference modeling of tsunami  
435 generation in a compressible ocean from offshore earthquakes. *Computational Geo-*  
436 *sciences*, 2015.
- 437 [30] Shuo Ma and Gregory C Beroza. Rupture dynamics on a bimaterial interface for dipping  
438 faults. *Bulletin of the Seismological Society of America*, 98(4):1642–1658, 2008.
- 439 [31] Shuo Ma and Evan T Hirakawa. Dynamic wedge failure reveals anomalous energy  
440 radiation of shallow subduction earthquakes. *Earth and Planetary Science Letters*,  
441 375:113–122, 2013.
- 442 [32] Seiichi Miura, Narumi Takahashi, Ayako Nakanishi, Tetsuro Tsuru, Shuichi Kodaira,  
443 and Yoshiyuki Kaneda. Structural characteristics off Miyagi forearc region, the Japan  
444 Trench seismogenic zone, deduced from a wide-angle reflection and refraction study.  
445 *Tectonophysics*, 407(3):165–188, 2005.

- 446 [33] Yasuyuki Nakamura, Shuichi Kodaira, Becky J Cook, Tamara Jeppson, Takafumi  
447 Kasaya, Yojiro Yamamoto, Yoshitaka Hashimoto, Mika Yamaguchi, Koichiro Obana,  
448 and Gou Fujie. Seismic imaging and velocity structure around the JFAST drill site in  
449 the Japan Trench: low  $V_p$ , high  $V_p/V_s$  in the transparent frontal prism. *Earth, Planets*  
450 *and Space*, 66(1):1–12, 2014.
- 451 [34] Ayako Nakanishi, Shuichi Kodaira, Seiichi Miura, Aki Ito, Takeshi Sato, Jin-Oh Park,  
452 Yukari Kido, and Yoshiyuki Kaneda. Detailed structural image around splay-fault  
453 branching in the Nankai subduction seismogenic zone: Results from a high-density  
454 ocean bottom seismic survey. *Journal of Geophysical Research: Solid Earth*, 113(B3),  
455 2008.
- 456 [35] Julie Pietrzak, Anne Socquet, David Ham, Wim Simons, Christophe Vigny, Robert Jan  
457 Labeur, Ernst Schrama, Guus Stelling, and Deepak Vatvani. Defining the source region  
458 of the Indian Ocean Tsunami from GPS, altimeters, tide gauges and tsunami models.  
459 *Earth and Planetary Science Letters*, 261(1):49–64, 2007.
- 460 [36] Jascha Polet and Hiroo Kanamori. Shallow subduction zone earthquakes and their  
461 tsunamigenic potential. *Geophysical Journal International*, 142(3):684–702, 2000.
- 462 [37] Hugues Raimbourg, Yozo Hamano, Saneatsu Saito, Masataka Kinoshita, and Achim  
463 Kopf. Acoustic and mechanical properties of Nankai accretionary prism core samples.  
464 *Geochemistry, Geophysics, Geosystems*, 12(4), 2011.
- 465 [38] Demian M Saffer and Chris Marone. Comparison of smectite-and illite-rich gouge fric-  
466 tional properties: application to the updip limit of the seismogenic zone along subduc-  
467 tion megathrusts. *Earth and Planetary Science Letters*, 215(1):219–235, 2003.
- 468 [39] Mariko Sato, Tadashi Ishikawa, Naoto Ujihara, Shigeru Yoshida, Masayuki Fujita,  
469 Masashi Mochizuki, and Akira Asada. Displacement above the hypocenter of the 2011  
470 Tohoku-Oki earthquake. *Science*, 332(6036):1395–1395, 2011.
- 471 [40] David W Scholl and Roland von Huene. Crustal recycling at modern subduction zones  
472 applied to the past—issues of growth and preservation of continental basement crust,  
473 mantle geochemistry, and supercontinent reconstruction. *Geological Society of America*  
474 *Memoirs*, 200:9–32, 2007.
- 475 [41] Mark Simons, Sarah E Minson, Anthony Sladen, Francisco Ortega, Junle Jiang, Susan E  
476 Owen, Lingsen Meng, Jean-Paul Ampuero, Shengji Wei, Risheng Chu, et al. The 2011

- 477 magnitude 9.0 Tohoku-Oki earthquake: Mosaicking the megathrust from seconds to  
478 centuries. *Science*, 332(6036):1421–1425, 2011.
- 479 [42] Keith Smith. *Environmental hazards: assessing risk and reducing disaster*. Routledge,  
480 2013.
- 481 [43] Seth Stein and Emile A Okal. Seismology: Speed and size of the Sumatra earthquake.  
482 *Nature*, 434(7033):581–582, 2005.
- 483 [44] Yuichiro Tanioka and Kenji Sataka. Fault parameters of the 1896 Sanriku tsunami  
484 earthquake estimated from tsunami numerical modeling. *Geophysical Research Letters*,  
485 23(13):1549–1552, 1996.
- 486 [45] Harold J Tobin and J Casey Moore. Variations in ultrasonic velocity and density with  
487 pore pressure in the decollement zone, northern Barbados Ridge accretionary prism. In  
488 *Proceedings of the Ocean Drilling Program. Scientific results*, pages 125–136. National  
489 Science Foundation, 1997.
- 490 [46] Harold J Tobin, J Casey Moore, and GF Moore. Laboratory measurement of velocity  
491 vs. effective stress in thrust faults of the Oregon accretionary prism: Implications for  
492 fault zone overpressure. In *Proceedings of the Ocean Drilling Program. Scientific results*,  
493 volume 146, pages 349–358. Ocean Drilling Program, 1995.
- 494 [47] Roland von Huene, Ingo A Pecher, and Marc-Andre Gutscher. Development of the  
495 accretionary prism along Peru and material flux after subduction of Nazca Ridge. *Tec-*  
496 *tonics*, 15(1):19–33, 1996.
- 497 [48] Roland von Huene and Cesar R Ranero. Subduction erosion and basal friction along  
498 the sediment-starved convergent margin off Antofagasta, Chile. *Journal of Geophysical*  
499 *Research: Solid Earth*, 108(B2), 2003.
- 500 [49] Roland von Huene, Cesar R Ranero, and Dave W Scholl. Convergent margin structure  
501 in high-quality geophysical images and current kinematic and dynamic models. In  
502 *Subduction Zone Geodynamics*, pages 137–157. Springer, 2009.
- 503 [50] Johannes Weertman. Unstable slippage across a fault that separates elastic media of  
504 different elastic constants. *Journal of Geophysical Research: Solid Earth*, 85(B3):1455–  
505 1461, 1980.